Research
Environmental Engineering—Article

Conversion Mechanism of Biomass to Nano Zero-Valent Iron Biochar: Iron Phase Transfer and *in Situ* Reduction

Sheng-Nan Zhuo, Hong-Yu Ren *, Guo-Jun Xie, De-Feng Xing, Bing-Feng Liu *

State Key Laboratory of Urban Water Resource and Environment, School of Environment, Harbin Institute of Technology, Harbin 150090, China

ABSTRACT

Nano zero-valent iron biochar (nZVI–BC), an environmentally-friendly functional material prepared from waste biomass, has attracted extensive attention. This material has potential to solve the problem of biomass conversion. However, the lack of a method of converting biomass to the nZVI–BC involved in biomass modification and pyrolysis hinders its further production and application. In this study, we introduced the green solvent polyethylene glycol 400 (PEG400) to a biomass (rice straw (RS)) modification system with $FeCl_3 \cdot 6H_2O$, and activated RS was prepared to nZVI–BC by one-step pyrolysis. The addition of PEG400 promoted the hydrolysis of iron ion and improved the RS surface structure, promoting the attachment of Fe_2O_3 to the RS surface. The mild activation conditions with temperatures of 60, 80, and 100 °C and a time of 0.5 h prevented the excessive loss of the lignin component and were conducive to the formation of carbon skeletons. Amorphous carbon and Fe_2O_3 were subjected to redox reactions to form nZVI–BC with the assistance of reducing gas produced from pyrolysis. In addition, the prepared nZVI–BC was tested for dye (Congo red) removal, showing rapid absorption (70.60% at 5 min) and high catalysis in advanced oxidation (75.67% at 5 min, 90.00% at 60 min). This work proposed a novel mechanistic strategy for preparing nZVI–BC and set a foundation for its scaled production and application.

© 2021 THE AUTHORS. Published by Elsevier LTD on behalf of Chinese Academy of Engineering and Higher Education Press Limited Company. This is an open access article under the CC BY-NC-ND license (http://creativecommons.org/licenses/by-nc-nd/4.0/).

1. Introduction

Hundreds of billion tons of lignocellulosic biomass are produced annually worldwide, but less than 10% of lignocellulosic biomass is utilized. The large production area and burning have caused serious environmental problems, and the transformation of waste biomass has attracted worldwide attention [1,2]. In addition to the saccharification of biomass to produce ethanol, many types of biomass are converted to carbon materials for environmental remediation [3]. Biochar (BC), which is carbonized from biomass under limited O_2 with high surface area, porosity, and rich functional groups, is widely applied in wastewater treatment as an environmentally friendly functional material [4]. To improve the degradation efficiency of BC on a greater number of pollutants, BC-loaded/supported nano zero-valent iron (nZVI) material has emerged. These composite materials of nZVI–BC have shown excellent removal efficiency in dye, heavy metal, and organic pollutant degradation [5–7].

nZVI–BC has been extensively studied for its potential application in environmental remediation. However, it is worth noting that many studies involve other iron phase components, such as Fe_2O_3 or Fe_3O_4, on nZVI–BC in addition to zero-valent iron (ZVI) [8,9]. These species mostly resulted from the incomplete reduction or oxidation of nZVI. Currently, there is a general preparation method for nZVI–BC, and it is broadly divided into two types: liquid reduction and carbothermal reduction. These methods are differentiated by the modified objects (biomass or BC), which are modified using iron salts. Liquid reduction adopted BC modification using reductants of borohydride (i.e., $NaBH_4$ or KBH_4) to reduce Fe^{3+} or Fe^{2+} to Fe^0 [10] onto the BC under N_2. The disadvantages of the process are that it is tedious and that Fe^0 is easily oxidized [11] and needs to be stored under vacuum [12]. In contrast, carbothermal reduction first adopted biomass modification via impregnation, and then the modified biomass was pyrolyzed to nZVI–BC [13]. Although this method makes up for the deficiency of the utilization of borohydride and N_2, it has some drawbacks, including the substantial use of Fe compounds and a long reaction time, which are related to the biomass structure.

Biomass is made of three major components: cellulose, hemicellulose, and lignin. They intertwine through strong covalent bonds

---

* Corresponding authors.
  E-mail addresses: rhy@hit.edu.cn (H.-Y. Ren), lbf@hit.edu.cn (B.-F. Liu).

and hydrogen bonds and result in the heterogeneity of the biomass [14,15]. In addition, lignin coats the outer layer of biomass, making the original biomass surface rigid and smooth and inaccessible to other substances [16]. Therefore, it is necessary to improve the surface accessibility by pretreatment to obtain the mixed carbon source of iron oxide and biomass before carbothermal reduction. Notably, studies have shown that graphitized carbon can shield iron nanoparticles against oxidation by acting as a "shell," and the metal Fe "core" provides strong support to prevent the collapse of the outer carbon shell [14]. Furthermore, the carbon skeleton was mainly derived from lignin, which comprises many aromatic rings and a wide pyrolysis range of 165–900 °C [17,18]. Thus, it is speculated that an improved nZVI–BC can be prepared through carbothermal reduction according to the following two ideas. The first is that during biomass modification, the biomass needs to be pretreated by inorganic iron compounds to retain more lignin. The second is that during pyrolysis, the Fe should be sufficiently reduced to ZVI when the biomass is pyrolyzed to graphitized carbon. However, limited studies have been performed on the detailed nZVI–BC formation mechanisms by carbothermal reduction involving prior iron activation and the formation of nZVI–BC using biomass as the carbon source.

Based on the numerous biomass pretreatment strategies (i.e., acid, alkali, and organic solvent methods) [19], lignin removal mechanism [20], and the traditional impregnation modification method (iron deposition) [21], we speculated that it is feasible to introduce a certain solvent to the heterogeneous modification system with biomass and iron salts to simultaneously weaken the pretreatment conditions (time, temperature, etc.) and improve the hydrolysis of the Fe ions; this system would satisfy the two goals of retaining lignin and enhancing the Fe deposition.

In this study, we first proposed an improved modification method to pretreat biomass (rice straw (RS)). We selected an environmentally friendly solvent, polyethylene glycol 400 (PEG400), as the additional catalyst for the RS modification system, which included $FeCl_3$ solution. PEG400 is a nontoxic linear polymer that is essentially nonvolatile [22]; PEG400 is regarded as a phase transfer catalyst and has the ability to separate and chelate metal ions in aqueous biphasic systems [23]. Then, nZVI–BC, which has a core–shell structure, was prepared by carbothermal reduction. The physicochemical properties of the nZVI–BC were explored by various characterization methods. The mechanisms of RS modification and nZVI–BC formation were elucidated through studies on the structural changes of RS, iron phase transfer and *in situ* reduction. Moreover, nZVI–BC was tested in a dye removal experiment, showing excellent absorption and catalysis. This study provides new insight into the formation of nZVI–BC, might drive the actual production and application of this material, and is significant for the conversion of biomass to carbon materials and environmental remediation.

2. Material and methods

2.1. Biomass and chemicals

RS was purchased from Wuchang, Heilongjiang Province, China. The RS was cut and crushed by a pulverizer and then passed through 40–100 mesh as feedstock biomass. Before use, the RS feedstock was washed to remove ash and then dried for the next experiment. Chemicals including PEG400 (analytical reagent (AR), $\geq$ 99.9%) and $FeCl_3 \cdot 6H_2O$ (AR, $\geq$ 99%) were obtained from Sinopharm Chemical Reagent Co., Ltd. (China). Ultrapure water was used in all the experiments.

2.2. Modification of RS

Dried RS was weighed into a round-bottom flask at a ratio of 5 wt% (m/v), and then PEG400 (with water of 1:1 (v/v)) and

$FeCl_3 \cdot 6H_2O$ (2.5%, m/v) solution were added to mix. The apparatus was placed in an oil bath with constant magnetic stirring in accordance with the designated temperature and time. After the reaction, solid–liquid separation was performed through vacuum filtration. Then, the solid RS residues were rinsed repeatedly to remove the PEG400 and extra $FeCl_3$ using plenty of water until the pH was neutral. The washed RS was dried in an oven at 60 °C for 24 h. The executed experiments were as follows: ① RS without pretreatment; ② RS pretreated by $FeCl_3 \cdot 6H_2O$ solution alone (80 °C, 1 h), and ③ RS pretreated by PEG400 with $FeCl_3 \cdot 6H_2O$ cosolvent (60/80/100 °C, 0.5 h). The collected samples from the above three pretreatments were named RS, F–RS, and PFx–RS, where x indicates pretreatment temperatures of 60, 80, and 100 °C.

2.3. Pyrolysis synthesis of nZVI–BC

The pretreated RS (RS, F–RS, and PFx–RS) was dried before pyrolysis. Then, they were added to a corundum ark and placed in a tube furnace with a flowing N_2 atmosphere at a temperature of 700 °C for 2 h and a heating rate of 5 °C·min^{-1}. When the pyrolysis process was completed and the BC was cooled to room temperature, the corresponding BC materials were obtained. They were ground, passed through a 0.154 mm mesh and stored in an airtight container for further use. The obtained BCs were named BC, FBC, and PFxBC, corresponding to the precursor samples of RS, F–RS, and PFx–RS, respectively, and the x in PFxBC still indicates the pretreatment temperatures of 60, 80 and 100 °C.

2.4. Biomass characterizations

To elucidate the formation mechanism of nZVI–BC, changes in RS before and after pretreatment were observed. Energy dispersive spectroscopy (EDS, Oxford, X-Max, UK) mapping was used to observe the element distribution and content changes, particularly the changes in the iron content. X-ray photoelectron spectroscopy (XPS, Kratos Axis Ultra DLD, UK) was also employed to investigate the chemical elements and ensure the iron phase compositions through overlapping peak resolution.

2.5. BC characterizations

The surface and inner morphology properties of BC were characterized by scanning electron microscopy (SEM, Zeiss Sigma 500, Germany) equipped with EDS and transmission electron microscopy (TEM, JEM1400, Japan). The phase composition was ensured by X-ray diffraction testing (XRD, Bruker D8 Advance, Germany). A vibrating sample magnetometer (VSM, Lake Shore 7404, USA) was used to monitor the magnetic intensity of nZVI–BC. The charge distribution on the surface of the nZVI–BC was measured by a zeta potential meter (Malvern Zetasizer Nano S90, UK). The surface element content and chemical valence changes were monitored using XPS. Fourier transform infrared spectroscopy (FTIR, PerkinElmer Spectrum One, USA) was used to analyze the functional groups of the BC. The specific surface area, pore volume, and pore size distribution were monitored by a N_2 absorption desorption isotherm (BET, Quantachrome NOVA Station B, Germany). The carbon structure and degree of graphitization were characterized by laser confocal Raman microspectroscopy (inVia-Reflex, UK) with an excitation wavelength of 532 nm at room temperature.

2.6. Congo red (CR) removal

The resultant nZVI–BC was used as a catalyst to advance the oxidation of persulfate for the removal of CR. The reaction conditions were as follows: CR concentration of 30 mg·L^{-1}, pH of 6.8 ± 0.2, reaction time of 0–150 min, dose of nZVI–BC of 0.5 g·L^{-1},

potassium peroxodisulfate ($K_2S_2O_8$; PS) concentration of 1.8 mmol·L^{-1}, reaction volume of 50 mL, and temperature of 30 °C. nZVI–BC and PS were added to the reactor at set proportions, and the bottle was placed into a water bath shaker. At the given irradiation time intervals, 500 μL of the solution was withdrawn, diluted, and centrifuged for 3 min at 8000 r·min^{-1}. Then, its absorption intensity was analyzed using a ultraviolet–visible (UV–vis) spectrophotometer (A360, Aoyi Instruments Shanghai Co., Ltd., China) at 498 nm. The removal efficiency of CR was calculated by the following expression:

$$CR \text{ removal efficiency} = \frac{C_0 - C_t}{C_0} \times 100\% \tag{1}$$

where C_0 and C_t are the initial and t min concentrations of CR (mg·L^{-1}) in the solution, respectively. After the reaction, the removal efficiency was studied by full wavelength scanning via UV–vis. For comparison, an experiment was conducted in which only PS was oxidized. Moreover, to distinguish the adsorption of nZVI–BC, experiments with nZVI–BC alone were carried out. The physicochemical property changes of nZVI–BC before and after use was analyzed by XRD, FTIR, and SEM equipped with EDS.

3. Results and discussion

3.1. Characteristics of the nZVI–BC

According to our designed experimental process, as shown in Appendix A Fig. S1, we first modified RS with a heating pretreatment in $FeCl_3$ solution (80 °C, 1 h) and a mixture of PEG400 and $FeCl_3$ (60/80/100 °C, 0.5 h) and then pyrolyzed the modified samples to obtain the corresponding materials, which were named FBC, PF60BC, PF80BC, and PF100BC.

3.1.1. Physical characteristics

(1) **XRD analysis.** The XRD spectra (Fig. 1(a)) of PF60BC, PF80BC, and PF100BC displayed characteristic peaks at ~44.7° corresponding to the typical (110) plane of Fe^0; these peaks are consistent with those in previous reports [24,25]. With increasing heating temperature, the peak became stronger and sharper, suggesting that the content of Fe^0 increased in the BC. Moreover, the diffraction peaks at 65.0° and 82.3°, which were indexed to the (200) and (211) planes of Fe^0, were present in the PF100BC pattern [26]. However, the FBC pattern did not exhibit the diffraction peak of Fe^0 as that of PFxBC, which also indicated that the single modification by $FeCl_3$ without PEG400 was inferior to the combined modification. It was confirmed that nZVI–BC was successfully fabricated in our synthesis process. Moreover, it is worth noting that there was another advantage of PFxBC in that its phase composition was pure. It was better than those of some similar materials reported in Refs. [8,9,12].

(2) **VSM analysis.** The VSM results (Fig. 1(b)) showed that PFxBC was magnetic; however, the FBC was barely magnetic. This trend is consistent with the XRD results. Combined with the phase analysis by XRD, it can be considered that the magnetism of the PFxBC resulted from Fe^0. The magnetic intensity of PFxBC gradually increased from PF60BC (3.00 emu·g^{-1}) to PF100BC (4.94 emu·g^{-1}), which was 4.57-fold that of FBC (1.08 emu·g^{-1}). Although the magnetic intensity was not as high as was shown in some other reports of iron oxide-dependent magnetic BC [27], it was still comparable to that of most reported magnetic BCs [28,29], and our nZVI–BC can be easily separated from a liquid phase system through magnetic force (it has been tested).

(3) **Raman analysis.** The Raman spectra (Fig. 1(c)) measured the carbon structure and degree of graphitization of the prepared BC. The peaks of the D mode (1360 cm^{-1}) and G mode (1590 cm^{-1})
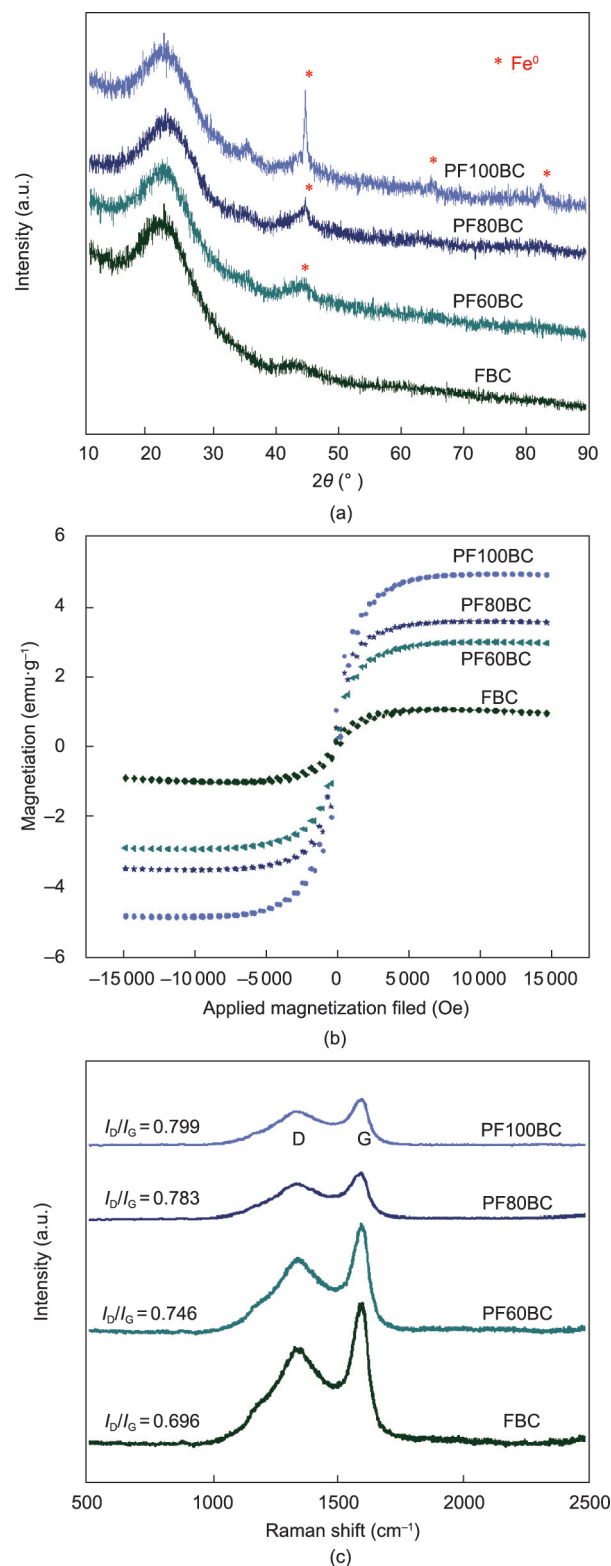

Fig. 1. (a) XRD, (b) VSM, and (c) Raman spectra of as-prepared BC. a.u.: arbitrary unit; 2θ: scattering angle.

were attributed to amorphous carbon and graphitic carbon, respectively [30]. The intensity ratio (I_D/I_G) increased from 0.696 for FBC to 0.746 for PF60BC, 0.783 for PF80BC, and 0.799 for PF100BC, indicating that the production of Fe^0 led to decreased graphitization of the prepared BC. With increasing Fe^0 intensity, I_D/I_G increased and introduced more disordered structures into nZVI–BC.

(4) **SEM and TEM analysis.** SEM images of the morphologies of the BC, FBC, and PF100BC are shown in Appendix A Fig. S2(a) and Figs. 2(a)–(c) for comparison. In particular, the surfaces of the BC (Fig. S2(a)) and FBC (Fig. 2(a)) were smooth and had few particles. In contrast, PF100BC (Figs. 2(b) and (c)) was embedded with a large number of white particles, and some bright particles were present on the surface. This observation was further confirmed by comparison with PF80BC (Fig. S2(b) in Appendix A), and the white particles in PF80BC framed by the green box were not as numerous as in the PF100BC. Through TEM (Fig. 2(d)) analysis, we confirmed that the large amounts of white particles growing inside PF100BC were nZVI particles, and this result was consistent with other studies [31,32]. In addition, the Fe^0 particles were on the nanoscale, with sizes below 100 nm. The white particles on the surface of PF100BC were believed to be other iron phase components, such as iron oxide; the presence of such particles was confirmed by XPS.

(5) **XPS analysis.** The element compositions of the prepared BCs were detected by XPS, and the results are listed in Appendix A Table S1, Figs. 2(e) and (f) and Appendix A Fig. S2(c). The content of Fe increased from BC (0.39%) to PF100BC (0.93%); this result was consistent with the XRD and VSM results. In addition, two typical satellite peaks at ~711 and ~724 eV were present in the spectra of FBC and PF100BC (Figs. 2(e) and (f)) and are believed to be the $2p_{3/2}$ and $2p_{1/2}$ satellite peaks from Fe_2O_3 [33,34]. Based on the results, the matter attached to the surface of FBC and PF100BC is likely to be Fe_2O_3. This compound might result from the incomplete reduction of Fe_2O_3 to Fe^0. Furthermore, the atomic percentage of Fe in the BC was equal to that in the FBC, but the signal peak of Fe_2O_3 did not appear in the BC (Figs. S2(b)), which might be due to the presence of iron on the surface of the RS as an elementary substance. Based on the above analysis, the nZVI–BC we prepared was composed of Fe^0 inside the BC and a small amount of Fe_2O_3 on the surface.

(6) **BET analysis.** N_2 adsorption/desorption isotherms and information on pore volume and sizes are shown in Figs. 2(g) and (h) and Appendix A Table S2. With the increasing introduction of Fe^0, the specific surface area (S_{BET}) increased and the pore size (D_p) decreased, which might be attributed to the occupation of

nano Fe^0 particles inside the BC [26], as concluded by XRD, SEM, and TEM analyses.

Compared to the BC and FBC, the PFxBC displayed increases in S_{BET} and total pore volume (V_{tot}) from 136 and 290 to 373 $m^2 \cdot g^{-1}$, and 0.1100 and 0.1610 to 0.2015 $cm^3 \cdot g^{-1}$, respectively, indicating the dispersion of Fe^0 inside the BC. Moreover, the D_p of the prepared BCs had small mesopores (2–4 nm), and there were no micropores in the BC. However, due to the modification of the RS, as Fe^0 was introduced, the micropore volume (V_{micro}) increased, indicating that some small pores were blocked by Fe^0 particles. Additionally, this result showed that it was better to modify the biomass to enhance its S_{BET} before pyrolysis to BC, as this modification is beneficial for their application.

In summary, nZVI–BC can be successfully prepared by our modification method, and the synthetic material has excellent characteristics. Compared with other preparation methods of nZVI–BC (listed in Table 1 [7–9,35,36]), our method has the advantages of simplicity, short time, low cost, and environmental friendliness without an extra reducing agent.

In addition, as shown in Appendix A Fig. S3, we monitored the stability of prepared PF100BC via zeta potential at various pH and by XRD at different times. The results indicated that PF100BC has excellent stability over a wide pH range. The surface of the material carried a large amount of negative charge when pH > 6. The XRD results demonstrated that the material exhibited high stability at 240 days. The typical diffraction peak intensity of the Fe^0 matched that of fresh Fe^0. No other oxidized substance was observed in the results.

In addition to the physical properties of nZVI–BC, the chemical structure was equally important. Information on the functional groups and chemical element species was obtained by FTIR and XPS (Fig. 3). Since BC and FBC were not composited with Fe^0, we selected PF100BC to conduct the contrast analysis with PFxBC.

3.1.2. Chemistry characteristics

(1) **FTIR analysis.** As shown in Fig. 3(a), the main bands in BC are as follows: a broad band at approximately 3433 cm^{-1} is the characteristic peak of O–H, and the band at 1617 cm^{-1} is assigned
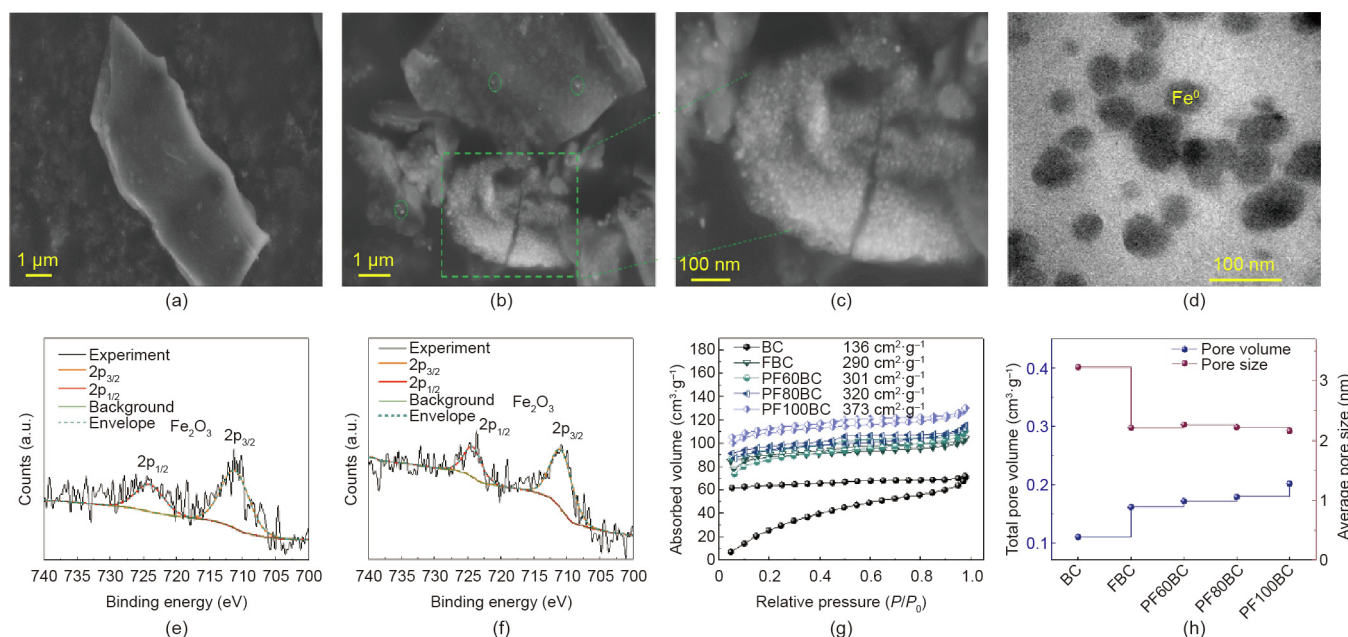

Fig. 2. SEM images of (a) FBC, (b, c) PF100BC; TEM of (d) PFBC; The high resolution Fe2p spectra of (e) FBC, (f) PF100BC; (g) N_2 adsorption and desorption isotherms of as-prepared BC; (h) pore volume and pore size of as-prepared samples. P_0: standard atmospheric pressure.

Table 1
Comparison of different nZVI–BC preparation methods.

| Name	Precursor	Preparation method	Detailed procedures	Source
nZVI@BC	Cornstalk	Liquid reduction	Pyrolysis at 500 °C for 2 h; soak in $FeCl_3 \cdot 6H_2O$ for 24 h; purge N_2 for 30 min; $NaBH_4$ reduction for 30 min	[35]
C–Fe^0	Carbon black	Carbonthermal reduction	$Fe(NO_3)_3 \cdot 9H_2O$ adsorption; vacuum dry; pyrolysis at 800 °C for 3 h under Ar atmosphere	[9]
BC-supported nZVI	RS	Liquid reduction	Pyrolysis at 500 and 700 °C; mix with $FeSO_4 \cdot 7H_2O$ to agitate for 24 h; purge N_2 for 1 h; KBH_4 reduction	[36]
Fe/C composites	Maize cob	Liquid reduction	Pyrolysis at 600 °C for 2 h; mix with $FeSO_4 \cdot 7H_2O$ to shake for 12 h; $NaBH_4$ reduction for 1 h under N_2 atmosphere	[7]
Fe^0@C	Glucose monohydrate	Carbonthermal reduction	Hydrothermal treatment using Fe_3O_4 at 180 °C for 10 h; pyrolysis at 700 °C for 2 h	[8]
nZVI–BC	RS	Carbonthermal reduction	Heat treatment using $FeCl_3 \cdot 6H_2O$ and PEG400 at 80 °C for 30 min; pyrolysis at 700 °C for 2 h	This study
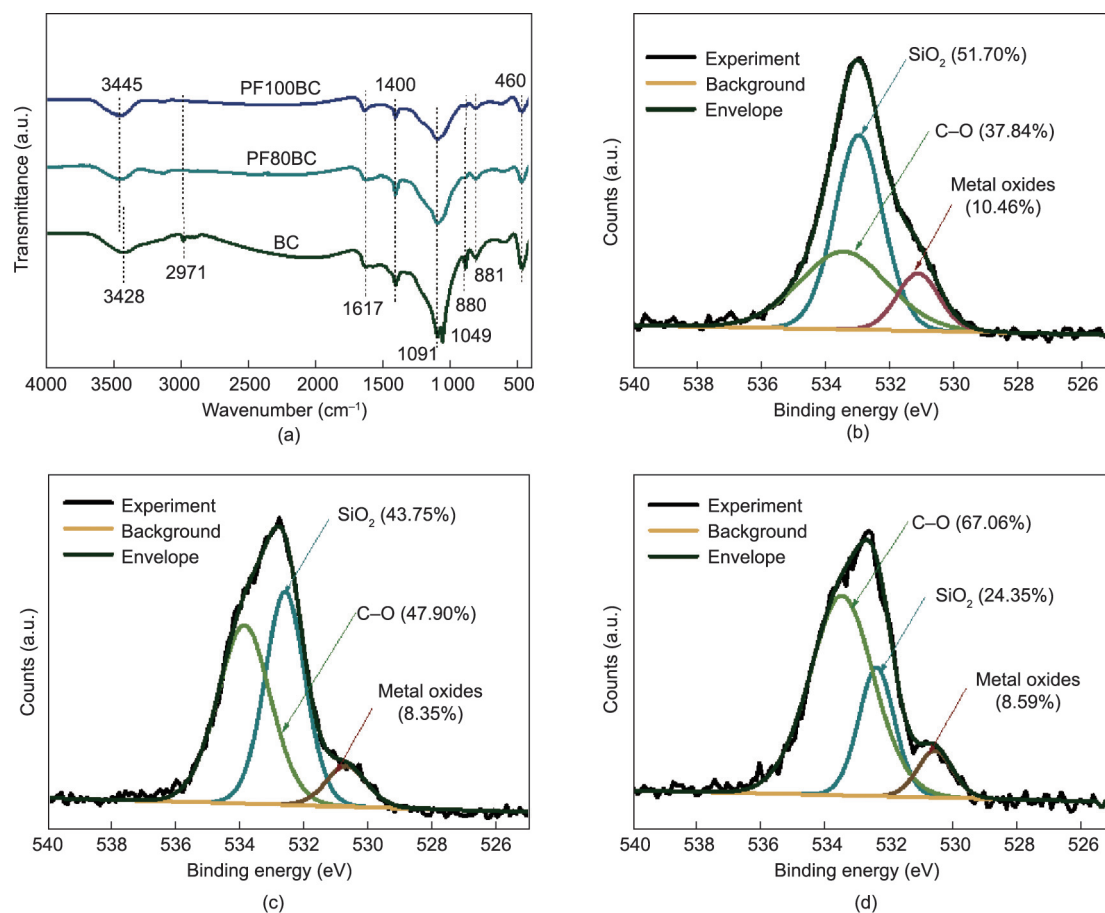
Fig. 3. (a) FTIR spectra of BC, PF80BC, and PF100BC; the high resolution XPS O1s spectra of (b) BC, (c) PF80BC, and (d) PF100BC.

to C=C and C=O stretching in the aromatic ring [37], the peak at 1400 cm^{-1} is indicative of the presence of –COO or a lactone structure [38], the peak at 1091 cm^{-1} is due to the C–O–C, the bands at 1049 and 801, 880 cm^{-1} are, respectively attributed to the asymmetric stretching of Si–O–Si and symmetric stretching of Si–O–Si, and the band at 460 cm^{-1} is due to the bending of O–Si–O [39].

Both organic and inorganic functional groups were present in the BC, as they were in a previous report [40]. However, the FTIR spectra of the nZVI–BC showed different variations. PF80BC and

PF100BC were found to show obvious changes at the positions of O–H and Si–O–Si and a weak difference in C=C. Based on the growth of the Fe^0 peak in the PF80BC and PF100BC spectra, it undoubtedly occupied some reaction sites on the BC. The Si–O–Si peaks at 880 and 1049 cm^{-1} were significantly decreased or eliminated, suggesting that a reaction occurred between Fe^0 and Si–O–Si, as occurred a previous study [36]. The O–H functional group shifted from 3428 to 3445 cm^{-1}; this shift was attributed to the effect of iron attachment [39]. In addition, the peaks indicating

C=C and C=O bonds in the aromatic ring, which appeared at 1617 cm^{-1}, were enhanced from a broad and irregular band to a strong and narrow peak. The exposed aromatic skeleton was derived from the lignin fractions of RS pyrolysis under high temperature because of the thermal destruction of cellulose and the aliphatic alkyl groups in the side chain [37].

FTIR analysis preliminarily demonstrated that the Fe^0 embedded inside the BC was bonded in the form of Si–O–Fe. It had a strong C=C skeleton, and the Fe^0 particles were dispersed inside the aromatic structure, avoiding aggregation and oxidation. To further determine the linked form of Fe^0 in nZVI–BC, the changes in the surface oxygen species of BC and PFxBC were detected by XPS.

(2) **XPS analysis.** Deconvoluting the XPS O 1s peak could help to identify the changes in prevalent oxygen species on the BC surface. The peaks at ~532.9, ~533, ~531, and ~530 eV correspond to SiO$_2$, organic C–O, metal carbonates and metal oxides [41]. Evidently, the dominant oxygen species was inorganic SiO$_2$ in BC (Fig. 3(b)), which had a relative abundance of 51.7%. This result can also be explained by XRD analysis of BC (Appendix A Fig. S4). Compared to those of other samples, the characteristic peaks of SiO$_2$ only occurred in the XRD patterns of BC, indicating the high content of SiO$_2$ in the BC. The SiO$_2$ in PF80BC and PF100BC decreased from 51.70% to 43.75% and 24.35%, respectively (Figs. 3(c) and (d)). This decrease was due to the production of Fe^0 particles, which reacted with the SiO$_2$, as described in the FTIR analysis. Additionally, the oxygen species of organic C–O of P80FBC and PF100BC increased from 37.84% to 47.90% and 67.06%, respectively, and were the dominant oxygen species. The results confirmed the changes in chemical composition, including inorganic Si–O–Si and organic C–O functional groups in terms of content, and identified the iron oxides that were present on the BC surface. As described in Figs. 3(c) and (d), the metal oxide peaks demonstrated the presence of Fe–O, which was corroborated the presence of Fe$_2$O$_3$ on the surface.

Thus, it can be concluded that nZVI–BC consists of Fe–O (Fe$_2$O$_3$) and Si–O (SiO$_2$) on the surface and Fe^0 within the core of the C=C (derived from lignin) skeleton/shell. This "core–shell" construction is favorable for protecting the Fe^0 from oxidation.

3.2. RS modification mechanism

The characteristics of the synthesized BCs indicated that the FeCl$_3$ modification of RS was enhanced by PEG400. To clarify the effect of PEG400 on RS modification, we explored the physico-chemical structure changes of RS before and after enhanced modification.

3.2.1. RS structure changes
As shown in Figs. 4(a)–(c), the surface of unmodified RS is rigid, and it has large amounts of lignin. After FeCl$_3$ modification, due to the acidic environment, the lignin was reordered and deposited on the F–RS surface in the form of droplets [36]. However, with the addition of PEG400, the structure of the PF80–RS became loose, and lignin was isolated by the solvolysis of the RS [42,43].

Additionally, the changes in RS from different modifications were reflected in the color and distribution of elements on their surface. It can be seen from Appendix A Fig. S5 that while the unmodified RS was yellow, the F–RS changed to black brown, and PF80–RS and PF100–RS were reddish-brown; this difference in color might result from the lignin or the mixture of lignin and iron oxide remaining on the surface of RS. In Refs. [44,45], biomass was pretreated with FeCl$_3$ under high temperature and high pressure, showing delignification, and the corresponding chemical group signals weakened. However, in this study, the FeCl$_3$ treatment conditions were normal pressure and temperatures below 100 °C. Thus, the treatment could not cause substantial lignin

removal or obvious changes in chemical structure, as displayed in the FTIR analysis (Appendix A Fig. S6).

In addition, EDS mapping pictures and energy spectra (Figs. 4(d)–(i)) showed that the content of Fe increased from 0.1% in RS and 0.3% in F–RS to 2.0% in PF80–RS, indicating that the introduction of PEG400 to the system was favorable for iron phase deposition. Moreover, the species of the iron phase were confirmed to be Fe$_2$O$_3$ by XPS (Fig. 5). Two typical satellite peaks occurred in F–RS and PF80–RS at positions of ~711 and ~724 eV, which were attributed to the 2p$_{3/2}$ and 2p$_{1/2}$ satellite peaks from Fe$_2$O$_3$. Clearly, the peak intensity of PF80–RS was stronger than that of F–RS. The Fe content was 3.33%, which was 9.4-fold higher than that of F–RS (0.32%). This result was in line with those of the EDS energy spectra. In addition, more Fe (5.47%) covered the PF100–RS, as listed in Appendix A Table S3, suggesting that the elevated temperature was better for the conversion of FeCl$_3$. This result supported the conjecture of color changes due to lignin and iron oxide.

Therefore, PEG400 played dual roles in the structural changes of RS and enhanced the production of Fe$_2$O$_3$ compared with RS modification by FeCl$_3$ alone.

3.2.2. Proposed iron phase transfer mechanism
PEG is a bifunctional amphiphilic polymer with reactive –OH groups on both ends [46], and it is usually considered a phase transfer catalyst [47]. The quantity of protons decreases as the amount of PEG increases in a liquid phase system [48]. In the RS system modified by FeCl$_3$, FeCl$_3$ could hydrolyze because of heating. Once Fe(OH)$_3$ was deposited on RS and dried, it was converted to Fe$_2$O$_3$, as shown in Eqs. (1) and (2):

$$FeCl_3 + H_2O \xrightarrow{\Delta} Fe(OH)_3 \downarrow + HCl \tag{2}$$

$$Fe(OH)_3 \xrightarrow{Dry} Fe_2O_3 \tag{3}$$

However, the hydrolysis of FeCl$_3$ under this condition might be weak, and it was restrained by the produced H$^+$. Thus, a small amount of Fe$_2$O$_3$ was detected in the F–RS (Figs. 4(h) and 5(e)). Adding PEG400 and increasing the temperature led to the consumption of H$^+$ [48] and promoted the positive movement of the hydrolysis reaction, and more Fe$_2$O$_3$ was produced (Figs. 4(i) and 5(f)).

Beyond that, the structural changes in RS caused by the addition of PEG400 also played an important role in the production of Fe$_2$O$_3$ on the surface of RS. After modification by FeCl$_3$, the F–RS surface was still rigid (Fig. 4(b)) and not conducive to the adsorption of Fe(OH)$_3$. However, the surface of PF–RS was rough and exposed cellulose, which might provide convenience for the adsorption of Fe(OH)$_3$, so more Fe$_2$O$_3$ was produced after drying.

Above all, it can be concluded that PEG400 led to increased hydrolysis of FeCl$_3$ to Fe(OH)$_3$, and the modification system enhanced the change in the RS surface structure, promoting the transfer of Fe(OH)$_3$ onto the RS and the production of Fe$_2$O$_3$. This result was important to Fe^0 formation in the following pyrolysis. We called the modification "iron phase transformation," and the proposed mechanism diagram is shown in Fig. 6.

3.3. Pyrolysis mechanism of modified RS to nZVI–BC

Fe^0 formation in the pyrolysis was mainly attributed to reduction by carbon and reducing gas (i.e., CO and H$_2$) [49], which were produced from biomass pyrolysis. The volatiles released from the pyrolysis of biomass play an important role in the reduction process [50]. Fe$_2$O$_3$ was reduced to Fe^0 with the help of these reducing gases. The type and output of reducing gas affected the quality of the reduction reaction. The release of gases depended on the pyrolysis temperature [51]. According to previous studies, we knew that
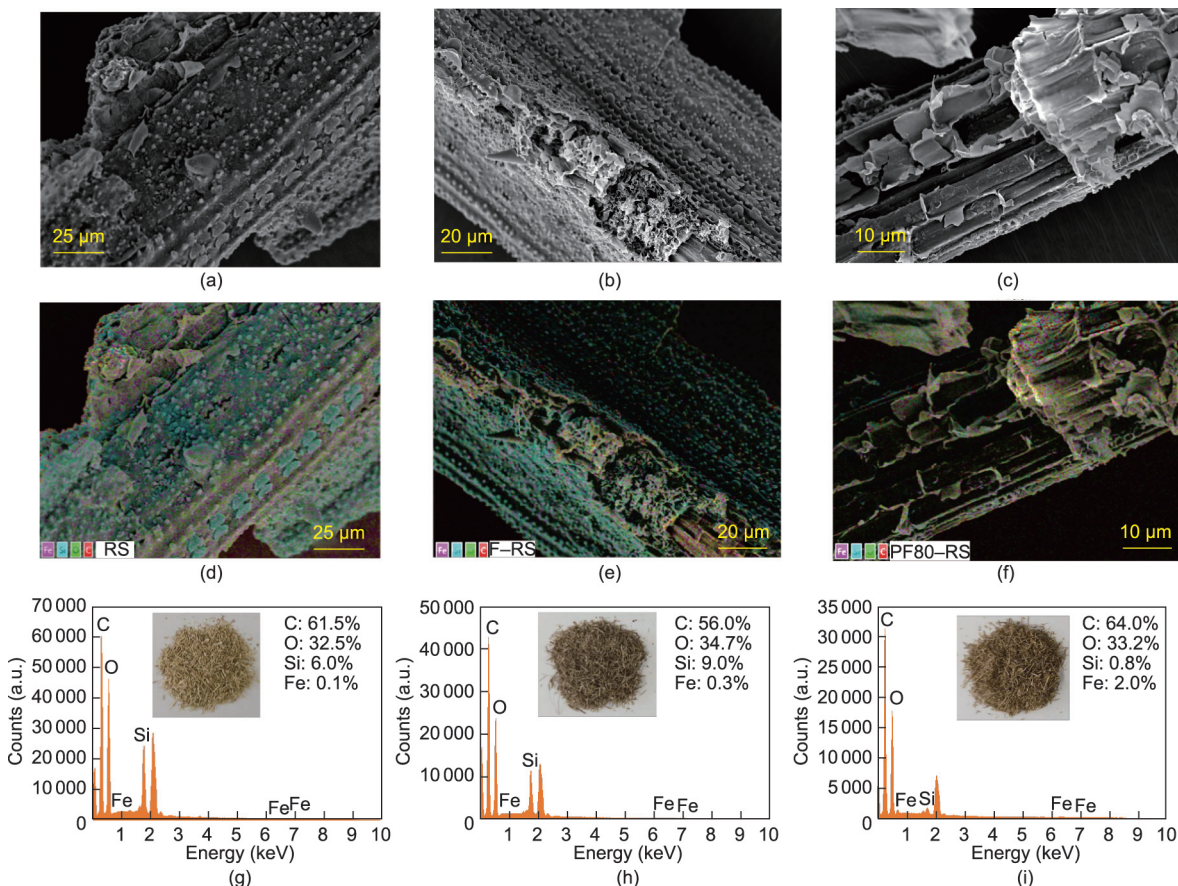
Fig. 4. SEM images of (a) RS, (b) F–RS, and (c) PF80–RS; EDS mapping of (d) RS, (e) F–RS, and (f) PF80–RS; EDS energy spectra and pictures of (g) RS, (h) F–RS, and (i) PF80–RS.
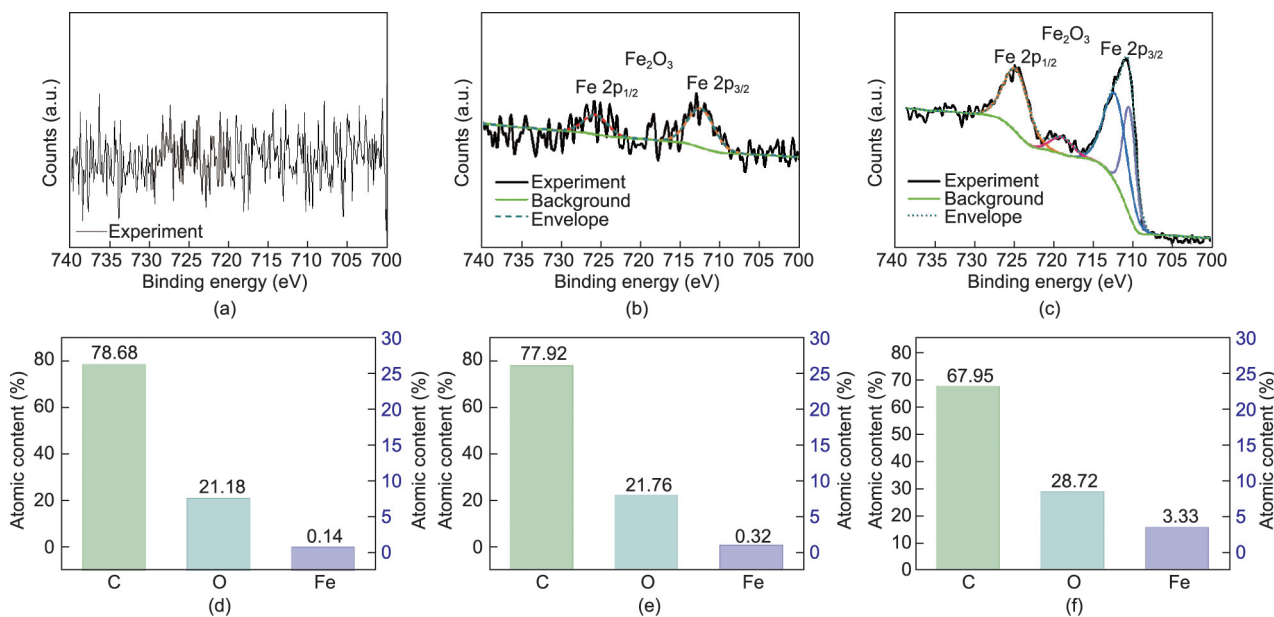

Fig. 5. The high resolution XPS Fe 2p spectra of (a) RS, (b) F–RS, and (c) PF80–RS; the percentage of element atomic content of (d) RS, (e) F–RS, and (f) PF80–RS.

CO was produced from hemicellulose over the whole pyrolysis temperature range. However, cellulose produced a relatively small amount of gas, while gas produced from lignin mainly occurred at temperatures higher than 600 °C [17]. CH_4 was mainly released from the C–C crack of lignin at 500–580 °C, and H_2 was mainly pro-

duced from breaking of the C–H bond as the temperature continued to increase [52].

FTIR spectra of PF100–RS and PF100BC are shown in Fig. 7, and assignments of absorption bands are shown in Appendix A Table S4 [15,53,54]. Visually, the main bands at 1384, 1245, 1163, 1061, and
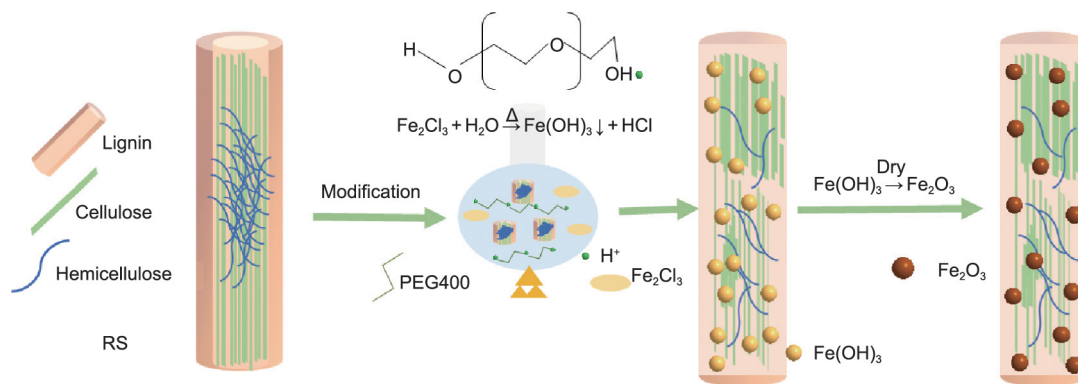
Fig. 6. Proposed iron phase transfer mechanism of enhanced FeCl$_3$ modification of RS by PEG400.
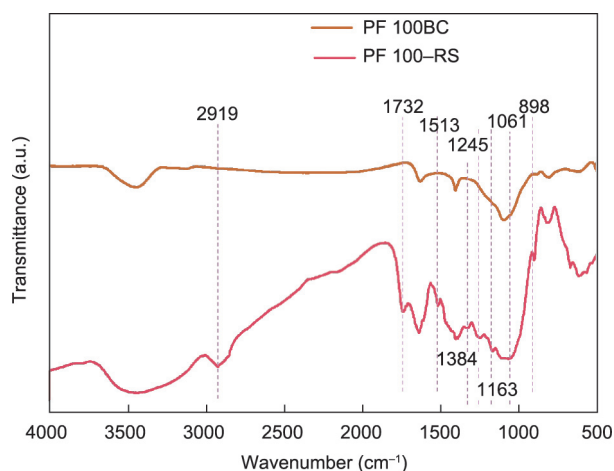

Fig. 7. FTIR spectra comparison of PF100–RS and PF100BC before and after pyrolysis.

898 cm^{-1} of cellulose and hemicellulose disappeared, indicating the breaking of the C–H, C–O, and C–O–C bonds. The bands related to the aromatic skeleton vibration of lignin only disappeared at 1513 cm^{-1}, suggesting that the breaking of the C–C bonds was not easy. This bond breakage led to the formation of a matrix structure of BC. The breakage of the C–O and C=O bonds at 1732 cm^{-1} mainly led to the formation of CO and CO$_2$. H$_2$ was produced from the breaking of C–H at 2919 and 1384 cm^{-1}. The small amount breaking of the C–C bonds resulted in a low CH$_4$ yield. Previous literature demonstrated that the gas yield would increase with increasing temperature [18]. As these gases formed, Fe$_2$O$_3$ reacted with them and was reduced to Fe^0. Notably, the temperature was set to 700 °C in this work; this temperature was higher than the abovementioned temperature. Moreover, the modified RS was not substantially destroyed. PEG400 only enhanced the production of Fe$_2$O$_3$ and improved the RS surface structure, and lignin was retained in the RS. Therefore, the modified RS could provide nearly all the necessary biomass components for gas production. Additionally, the reduction of Fe$_2$O$_3$ by CO and H$_2$ to produce Fe^0 would result in two intermediates, Fe$_3$O$_4$ and FeO (at temperatures above 570 °C) [14]. Under these conditions, Fe$_2$O$_3$ can be reduced to Fe^0 under enough reducing gases. The formation of Fe^0 was explained by Eqs. (4)–(9).

$$CO + 3Fe_2O_3 \rightarrow 2Fe_3O_4 + CO_2 \tag{4}$$

$$CO + Fe_3O_4 \rightarrow 3FeO + CO_2 \tag{5}$$

$$CO + FeO \rightarrow Fe + CO_2 \tag{6}$$

$$H_2 + 3Fe_2O_3 \rightarrow 2Fe_3O_4 + H_2O \tag{7}$$

$$H_2 + Fe_3O_4 \rightarrow 3FeO + H_2O \tag{8}$$

$$H_2 + FeO \rightarrow Fe + H_2O \tag{9}$$

Furthermore, to investigate whether Fe$_2$O$_3$ can be reduced to Fe^0 at lower pyrolysis temperatures, we used PF80–RS and PF100–RS to carry out pyrolysis experiments at 500 °C for comparison. The result was detected by XRD (Appendix A Fig. S7). The diffraction peak of Fe^0 at ~44.7° was absent, indicating that the gases released from pyrolysis at 500 °C were not enough to completely reduce Fe$_2$O$_3$ to Fe^0. Some reports have demonstrated that as the temperature increased, CO, CH$_4$, and H$_2$ were generated or increased [51]. Therefore, if we want to form BC with Fe^0 by carbothermal reduction, an appropriate pyrolysis temperature is crucial. This result was consistent with those of previous studies [49].

In addition to the low yield of gas production caused by low temperature (500 °C), carbon also played a role in the reduction of Fe$_2$O$_3$. The iron reduction process has been known to occur in gaseous phases such as CO and H$_2$ rather than reaction on solid carbon materials [55]. Carbon can affect the reduction of CO$_2$ according to Eq. (10).

$$CO_2 + C = 2CO \tag{10}$$

During pyrolysis, CO$_2$ was mainly produced at low temperature (< 500 °C) from hemicellulose at a high temperature (> 500 °C) [17]. As shown in the XPS spectra (Appendix A Fig. S8) and Appendix A Table S5, the O/C ratios of PF80BC and PF100BC decreased from 0.120 and 0.130 to 0.110 and 0.086, respectively, at 500 and 700 °C. The sp^2-C at ~284.4 eV and sp^3-C at ~285.0 eV (Appendix A Figs. S8(a) and (b)) in the carbon material increased (from 36.19% to 47.77% and 36.31% to 55.68%) and decreased (from 38.19% to 32.94% and 37.25% to 27.72%), respectively, indicating that the degree of graphitization of nZVI–BC improved [56]. This result might be due to the amorphous carbon involved in the reduction of CO$_2$; the produced CO continued to participate in the reduction of Fe$_2$O$_3$ to Fe^0 according to Eqs. (4)–(6).

In this study, Fe^0 was obtained by *in situ* carbothermic reduction, decreasing the release of greenhouse gases and environmental pollution; thus, this nZVI–BC preparation method can be regarded as a green production process. To better explain the formation of iron, the mechanism diagram is shown in Fig. 8.
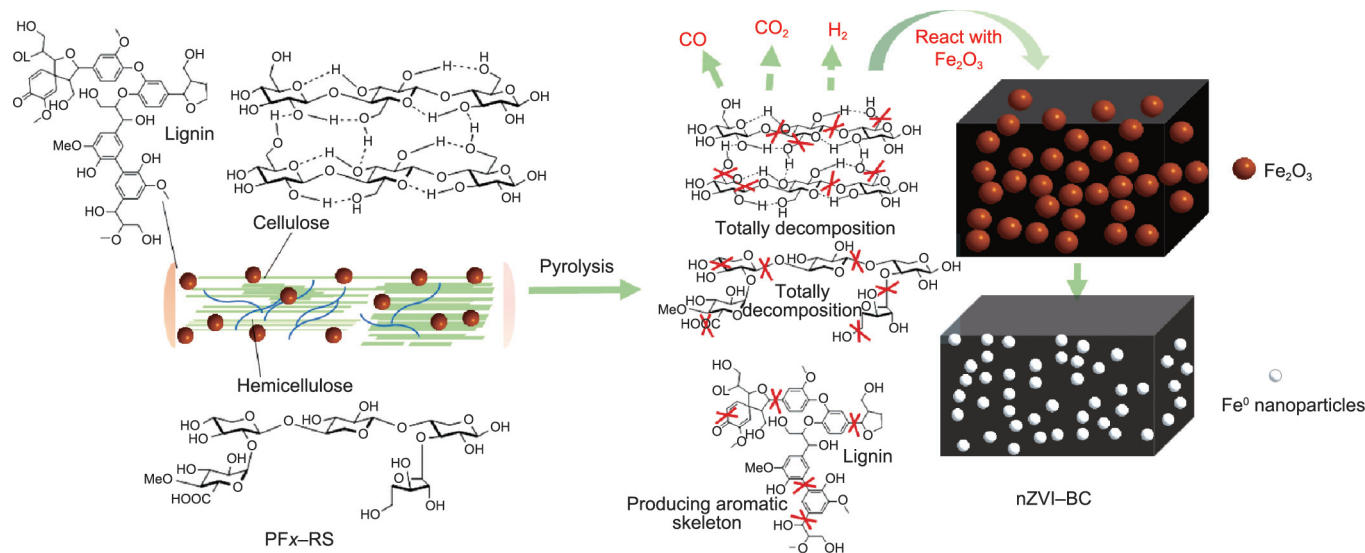
Fig. 8. Schematic pyrolysis process of nZVI–BC.

3.4. Application test of nZVI–BC in CR removal

To confirm the ability of PF100BC (that is, nZVI–BC) to remove pollution, we conducted an advanced catalytic oxidation experiment of CR, employing PF100BC as a catalyst. Control experiments of PS oxidation and PF100BC absorption alone were also performed.

3.4.1. CR removal analysis

As shown in Figs. 9(a) and (b), compared with that of oxidation using PS alone, the removal rate of PF100BC for CR increased sharply. During the same monitoring time, the remaining concentra-tion of CR using PF100BC as a catalyst was much lower than that without using PF100BC, indicating that PF100BC had performed the CR removal by advanced oxidation. The catalytic effect of PF100BC was satisfying. Within 5 min, PF100BC showed a highly efficient absorption ability of 70.6%. Additionally, the concentration of CR decreased from 30.0 to 7.3 $mg \cdot L^{-1}$, and the removal rate reached 75.67% by advanced catalytic oxidation with PF100BC. However, at this point, the removal rate of CR by PS oxidation alone was 4.3%. Therefore, under the catalysis of PF100BC, the oxidation efficiency of CR increased 17.6-fold. At 60 min, the CR concentration decreased to 3.0 $mg \cdot L^{-1}$, and the removal rate reached 90%. However, the absorption removal of CR by PF100BC was as low
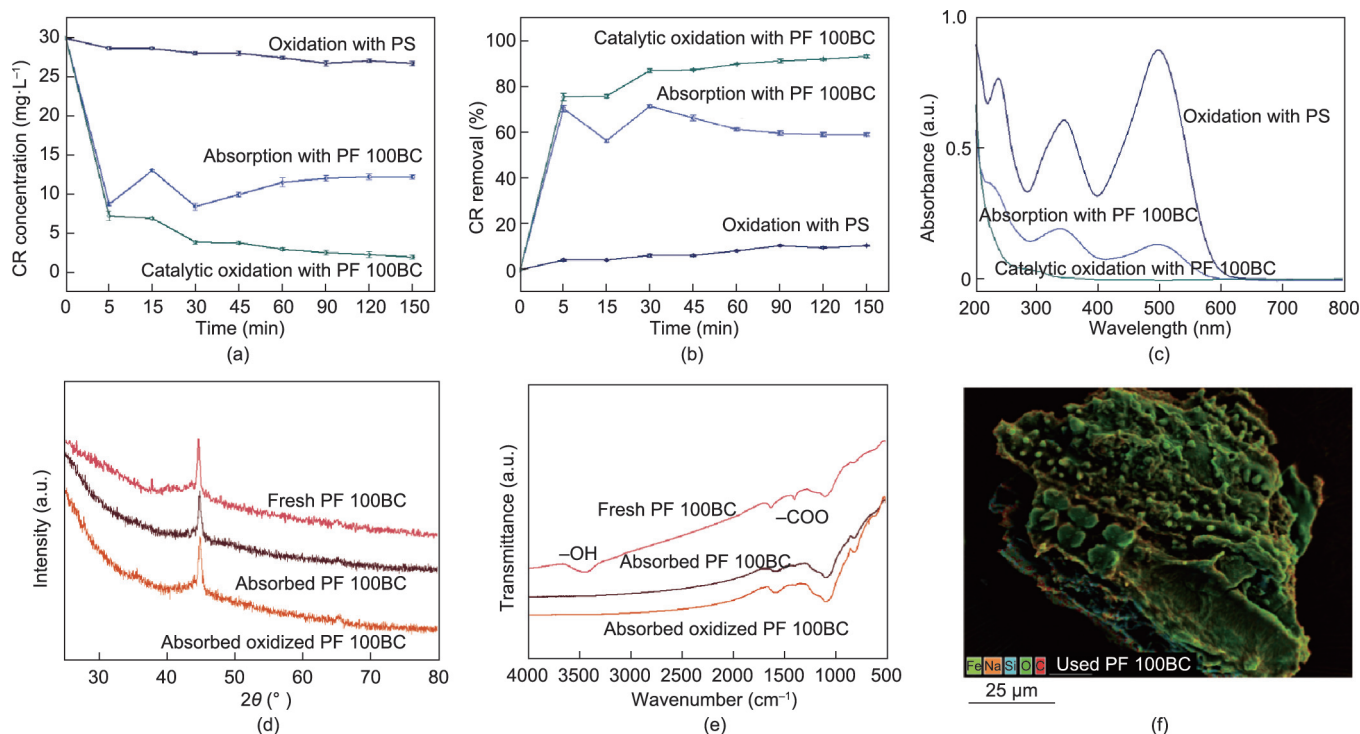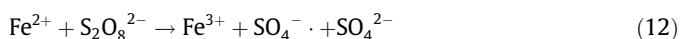

Fig. 9. Catalysis oxidation experiment of CR removal. (a) Degradation behavior of CR under different time by three methods; (b) CR removal efficiency under different conditions; (c) UV–vis scanning of CR after three removal approaches; (d) XRD spectra of fresh and used PF100BC by absorption and catalytic oxidation; (e) FTIR spectra of fresh and used PF100BC by absorption and catalytic oxidation; (f) EDS mapping image of used PF100BC by catalytic oxidation. Experimental conditions: CR 30.0 $mg \cdot L^{-1}$, PF100BC 0.5 $g \cdot L^{-1}$, PS 1.8 $mmol \cdot L^{-1}$, temperature 30 °C.

as 61.3%, which might be due to the desorption of PF100BC. The oxidation efficiency of CR by PS was just 8.3%, indicating that the advanced oxidation reaction was slow without the activation of nZVI. Moreover, as shown in Appendix A Fig. S9, the modeling results demonstrated that the catalytic degradation of CR by PF100BC complied with pseudo-first-order kinetics [57].

In addition, wavelength scanning of the CR solution was performed after the three reactions (Fig. 9(c)). After the oxidation of PS, the CR still had distinct absorbance peaks at 498 nm. After the absorption of nZVI–BC, the peak decreased, but the chromogenic absorption peak did not disappear. After advanced oxidation with PF100BC, the peak disappeared, demonstrating that the cleavage of the azo chromophore from CR might be related to nZVI [58].

3.4.2. The role of nZVI–BC on CR removal

To explore the effect of PF100BC on CR removal, the XRD spectra (Fig. 9(d)) of fresh and used PF100BC were monitored. They were nearly unchanged, and only the peak of ZVI decreased after use, which was attributed to the reaction of ZVI and $S_2O_8^{2-}$ (Eqs. (11) and (12)). Due to the formation of $SO_4^-\cdot$, CR was decolored and degraded quickly.

$$Fe^0 + S_2O_8^{2-} \rightarrow Fe^{2+} + 2SO_4^{2-} \tag{11}$$

$$Fe^{2+} + S_2O_8^{2-} \rightarrow Fe^{3+} + SO_4^-\cdot + SO_4^{2-} \tag{12}$$

The FTIR spectra (Fig. 9(e)) displayed different results. The bands of –COO and –OH disappeared after absorption and catalytic oxidation. This disappearance might be due to the –COO and –OH groups forming hydrogen bonds with dye anions of –NH$_2$ [59]. Thus, rapid adsorption was demonstrated. From the results of unstable absorption and increased advanced catalytic oxidation, it could be explained the CR was absorbed on the PF100BC relying on the bonding of functional groups, simultaneously degraded by the $SO_4^-\cdot$ generated from the activation of $S_2O_8^{2-}$ via Fe^0, with the electron transfer [28,35]. The mapping picture (Fig. 9(f)) of the nZVI–BC after advanced oxidation showed the presence of iron oxide on its surface, indicating the redox reaction of Fe^0. Throughout the whole process, absorption promoted the advanced oxidation degradation of CR [33].

In summary, the PF100BC prepared by our method displayed a quick and excellent ability to be applied in dye removal as a catalyst. Experiments to determine the optimal conditions for the efficient, advanced oxidation of CR, such as the dose of PF100BC, initial CR concentration, and pH of the CR solution, are being conducted. Further investigations on the detailed electron transfer mechanism of ZVI, free radical mechanism of $\cdot$OH or O_2^- and CR degradation pathway are being studied.

4. Conclusions

In this work, RS was modified by the improved strategy of introducing PEG400 into the FeCl$_3$ reaction system, and the modified RS was successfully prepared to magnetic nZVI–BC by carbon thermal reduction. In the RS modification, PEG400 promoted the hydrolysis of FeCl$_3$ and improved the RS surface structure, realizing the production of Fe$_2$O$_3$ on the RS surface. In the later pyrolysis process, carbonized RS and Fe$_2$O$_3$ underwent a redox reaction with reducing gas participation to form nZVI–BC. The obtained magnetic nZVI–BC was pure, and Fe^0 was embedded inside the carbon skeleton, protecting it from oxidation. nZVI–BC was tested for the advanced oxidation of CR, exhibiting a rapid absorption of 70.6% within 5 min and highly efficient catalytic degradation of 90% removal at 60 min. The novel modification method we proposed is simple, low-cost, time-saving, and environmentally friendly.

This study has significant implications for guiding the conversion of biomass to BC and great potential to drive the scale production of nZVI–BC, which is expected to be applied in batches for environmental remediation in the future.

Compliance with ethical guidelines

Sheng-Nan Zhuo, Hong-Yu Ren, Guo-Jun Xie, De-Feng Xing, and Bing-Feng Liu declare that they have no conflicts of interest or financial conflicts to disclose.

Appendix A. Supplementary data

Supplementary data to this article can be found online at https://doi.org/10.1016/j.eng.2021.07.012.

References

[1] Liu W, Jiang H, Yu H. Development of biochar-based functional materials: toward a sustainable platform carbon material. Chem Rev 2015;115:12251–85.
[2] Xiao Q, Chen W, Tian D, Shen F, Hu J, Long L, et al. Integrating the bottom ash residue from biomass power generation into anaerobic digestion to improve biogas production from lignocellulosic biomass. Energy Fuels 2020;34:1101–10.
[3] Jiang SF, Sheng GP, Jiang H. Advances in the characterization methods of biomass pyrolysis products. ACS Sustain Chem Eng 2019;7:12639–55.
[4] Zhong D, Jiang Y, Zhao Z, Wang L, Chen J, Ren S, et al. pH dependence of arsenic oxidation by rice-husk-derived biochar: roles of redox-active moieties. Environ Sci Technol 2019;53:9034–44.
[5] Xu W, Li Z, Shi S, Qi J, Cai S, Yu Y, et al. Carboxymethyl cellulose stabilized and sulfidated nanoscale zero-valent iron: characterization and trichloroethene dechlorination. Appl Catal B Environ 2020;262:118303.
[6] Liu Z, Zhang F. Nano-zerovalent iron contained porous carbons developed from waste biomass for the adsorption and dechlorination of PCBs. Bioresour Technol 2010;101:2562–4.
[7] Li Z, Sun Y, Yang Y, Han Y, Wang T, Chen J, et al. Biochar-supported nanoscale zero-valent iron as an efficient catalyst for organic degradation in groundwater. J Hazard Mater 2020;383:121240.
[8] Li S, Tang J, Liu Q, Liu X, Gao B. A novel stabilized carbon-coated nZVI as heterogeneous persulfate catalyst for enhanced degradation of 4-chlorophenol. Environ Int 2020;138:105639.
[9] Hoch LB, Mack EJ, Hydutsky BW, Hershman JM, Skluzacek JM, Mallouk TE. Carbothermal synthesis of carbon-supported nanoscale zero-valent iron particles for the remediation of hexavalent chromium. Environ Sci Technol 2008;42:2600–5.
[10] Vilardi G, Verdone N, Bubbico R. Combined production of metallic-iron nanoparticles: exergy and energy analysis of two alternative processes using Hydrazine and NaBH$_4$ as reducing agents. J Taiwan Inst Chem E 2021;118:97–111.
[11] Vilardi G, Verdone N. Production of metallic iron nanoparticles in a baffled stirred tank reactor: optimization via computational fluid dynamics simulation. Particuology 2020;52:83–96.
[12] Su Y, Cheng Y, Shih YH. Removal of trichloroethylene by zerovalent iron/activated carbon derived from agricultural wastes. J Environ Manage 2013;129:361–6.
[13] L'vov BV. Mechanism of carbothermal reduction of iron, cobalt, nickel and copper oxides. Thermochim Acta 2000;360:109–20.
[14] Neeli ST, Ramsurn H. Synthesis and formation mechanism of iron nanoparticles in graphitized carbon matrices using biochar from biomass model compounds as a support. Carbon 2018;134:480–90.
[15] Guo X, Zhang T, Shu S, Zheng W, Gao M. Compositional and structural changes of corn cob pretreated by electron beam irradiation. ACS Sustain Chem Eng 2017;5:420–5.
[16] Zhuo S, Yan X, Liu D, Si M, Zhang K, Liu M, et al. Use of bacteria for improving the lignocellulose biorefinery process: importance of pre-erosion. Biotechnol Biofuels 2018;11:146.

[17] Yang H, Yan R, Chen H, Lee DH, Zheng C. Characteristics of hemicellulose, cellulose and lignin pyrolysis. Fuel 2007;86:1781–8.

[18] Wang S, Dai G, Yang H, Luo Z. Lignocellulosic biomass pyrolysis mechanism: a state-of-the-art review. Prog Energy Combust Sci 2017;62:33–86.

[19] Agbor VB, Cicek N, Sparling R, Berlin A, Levin DB. Biomass pretreatment: fundamentals toward application. Biotechnol Adv 2011;29:675–85.

[20] Chundawat SPS, Donohoe BS, da Costa SL, Elder T, Agarwal UP, Lu F, et al. Multi-scale visualization and characterization of lignocellulosic plant cell wall deconstruction during thermochemical pretreatment. Energy Environ Sci 2011;4:973.

[21] Ahmed MB, Zhou JL, Ngo HH, Guo W, Chen M. Progress in the preparation and application of modified biochar for improved contaminant removal from water and wastewater. Bioresour Technol 2016;214:836–51.

[22] Chen J, Spear SK, Huddleston JG, Holbrey JD, Swatloski RP, Rogers RD. Application of poly(ethylene glycol)-based aqueous biphasic systems as reaction and reactive extraction media. Ind Eng Chem Res 2004;43:5358–64.

[23] Rogers RD, Bond AH, Bauer CB. Metal ion separations in polyethylene glycol-based aqueous biphasic systems. Sep Sci Technol 1993;28:1091–126.

[24] Zhu K, Xu H, Chen C, Ren X, Alsaedi A, Hayat T. Encapsulation of Fe^0-dominated $Fe_3O_4/Fe^0/Fe_3C$ nanoparticles into carbonized polydopamine nanospheres for catalytic degradation of tetracycline via persulfate activation. Chem Eng J 2019;372:304–11.

[25] Chen L, Feng S, Zhao D, Chen S, Li F, Chen C. Efficient sorption and reduction of U(VI) on zero-valent iron-polyanilinegraphene aerogel ternary composite. J Colloid Interf Sci 2017;490:197–206.

[26] Jiang X, Guo Y, Zhang L, Jiang W, Xie R. Catalytic degradation of tetracycline hydrochloride by persulfate activated with nano Fe^0 immobilized mesoporous carbon. Chem Eng J 2018;341:392–401.

[27] Zhang M, Gao B, Varnoosfaderani S, Hebard A, Yao Y, Inyang M. Preparation and characterization of a novel magnetic biochar for arsenic removal. Bioresour Technol 2013;130:457–62.

[28] Yu J, Tang L, Pang Y, Zeng G, Wang J, Deng Y, et al. Magnetic nitrogen-doped sludge-derived biochar catalysts for persulfate activation: internal electron transfer mechanism. Chem Eng J 2019;364:146–59.

[29] Wang J, Shao X, Tian G, Li Z, Bao W. Preparation and properties of α-Fe microparticles with high stability. Mater Lett 2017;192:36–9.

[30] Ferrari AC, Rodil SE, Robertson J. Interpretation of infrared and Raman spectra of amorphous carbon nitrides. Phys Rev B 2003;67:155306.

[31] He F, Zhao D. Manipulating the size and dispersibility of zerovalent iron nanoparticles by use of carboxymethyl cellulose stabilizers. Environ Sci Technol 2007;41:6216–21.

[32] Krajangpan S, Kalita H, Chisholm BJ, Bezbaruah AN. Iron nanoparticles coated with amphiphilic polysiloxane graft copolymers: dispersibility and contaminant treatability. Environ Sci Technol 2012;46:10130–6.

[33] Gong J, Yao K, Liu J, Jiang Z, Chen X, Wen X, et al. Striking influence of Fe_2O_3 on the "catalytic carbonization" of chlorinated poly(vinyl chloride) into carbon microspheres with high performance in the photo-degradation of Congo red. J Mater Chem A 2013;1:5247.

[34] Sun Y, Zhang Z, Sun Y, Yang G. One-pot pyrolysis route to Fe−N-Doped carbon nanosheets with outstanding electrochemical performance as cathode materials for microbial fuel cell. Int J Agric Biol Eng 2020;13:2017–114.

[35] Dong H, Deng J, Xie Y, Zhang C, Jiang Z, Cheng Y, et al. Stabilization of nanoscale zero-valent iron (nZVI) with modified biochar for Cr(VI) removal from aqueous solution. J Hazard Mater 2017;332:79–86.

[36] Qian L, Zhang W, Yan J, Han L, Chen Y, Ouyang D, et al. Nanoscale zero-valent iron supported by biochars produced at different temperatures: synthesis mechanism and effect on Cr(VI) removal. Environ Pollut 2017;223:153–60.

[37] Chen B, Zhou D, Zhu L. Transitional adsorption and partition of nonpolar and polar aromatic contaminants by biochars of pine needles with different pyrolytic temperatures. Environ Sci Technol 2008;42:5137–43.

[38] Zhu Y, Li H, Zhang G, Meng F, Li L, Wu S. Removal of hexavalent chromium from aqueous solution by different surface-modified biochars: acid washing, nanoscale zero-valent iron and ferric iron loading. Bioresour Technol 2018;261:142–50.

[39] Li Y, Jin Z, Li T. A novel and simple method to synthesize SiO_2-coated Fe nanocomposites with enhanced Cr(VI) removal under various experimental conditions. Desalination 2012;288:118–25.

[40] Qian L, Chen B. Dual role of biochars as adsorbents for aluminum: the effects of oxygen-containing organic components and the scattering of silicate particles. Environ Sci Technol 2013;47:8759–68.

[41] Yang J, Zhao Y, Ma S, Zhu B, Zhang J, Zheng C. Mercury removal by magnetic biochar derived from simultaneous activation and magnetization of sawdust. Environ Sci Technol 2016;50:12040–7.

[42] Nge TT, Tobimatsu Y, Takahashi S, Takata E, Yamamura M, Miyagawa Y, et al. Isolation and characterization of polyethylene glycol (PEG)-modified glycol lignin via PEG solvolysis of softwood biomass in a large-scale batch reactor. ACS Sustain Chem Eng 2018;6:7841–8.

[43] Li H, Wang C, Xiao W, Yang Y, Hu P, Dai Y, et al. Dissecting the effect of polyethylene glycol on the enzymatic hydrolysis of diverse lignocellulose. Int J Biol Macromol 2019;131:676–81.

[44] Wu X, Huang C, Tang W, Huang C, Lai C, Yong Q. Use of metal chlorides during waste wheat straw autohydrolysis to overcome the self-buffering effect. Bioresour Technol 2018;268:259–65.

[45] Chen L, Chen R, Fu S. $FeCl_3$ pretreatment of three lignocellulosic biomass for ethanol production. ACS Sustain Chem Eng 2015;3:1794–800.

[46] Lee CC, Doong RA. Enhanced dechlorination of tetrachloroethylene by zerovalent silicon in the presence of polyethylene glycol under anoxic conditions. Environ Sci Technol 2011;45:2301–7.

[47] Chen J, Spear SK, Huddleston JG, Rogers RD. Polyethylene glycol and solutions of polyethylene glycol as green reaction media. Green Chem 2005;7:64.

[48] Guilminot E, Dalard F, Degrigny C. Mechanism of iron corrosion in water–polyethylene glycol (PEG 400) mixtures. Corros Sci 2002;44:2199–208.

[49] Crane RA, Scott TB. Nanoscale zero-valent iron: future prospects for an emerging water treatment technology. J Hazard Mater 2012;211–2:112–25.

[50] Zhang H, Ruan Y, Liang A, Shih K, Diao Z, Su M, et al. Carbothermal reduction for preparing nZVI/BC to extract uranium: insight into the iron species dependent uranium adsorption behavior. J Clean Prod 2019;239:117873.

[51] Siengchum T, Isenberg M, Chuang SSC. Fast pyrolysis of coconut biomass—an FTIR study. Fuel 2013;105:559–65.

[52] Kan T, Strezov V, Evans TJ. Lignocellulosic biomass pyrolysis: a review of product properties and effects of pyrolysis parameters. Renew Sustain Energy Rev 2016;57:1126–40.

[53] Meng X, Sun Q, Kosa M, Huang F, Pu Y, Ragauskas AJ. Physicochemical structural changes of poplar and switchgrass during biomass pretreatment and enzymatic hydrolysis. ACS Sustain Chem Eng 2016;4:4563–72.

[54] Hao N, Bezerra TL, Wu Q, Ben H, Sun Q, Adhikari S, et al. Effect of autohydrolysis pretreatment on biomass structure and the resulting bio-oil from a pyrolysis process. Fuel 2017;206:494–503.

[55] Fruehan RJ. The Rate of reduction of iron oxides by carbon. Metall Trans B Process Metall 1977;8:279–86.

[56] Zhang K, Liu M, Zhang T, Min X, Wang Z, Chai L, et al. High-performance supercapacitor energy storage using a carbon material derived from lignin by bacterial activation before carbonization. J Mater Chem A 2019;7:26838–48.

[57] Di Palma L, Verdone N, Vilardi G. Kinetic modeling of Cr(VI) reduction by nZVI in soil: the influence of organic matter and manganese oxide. Bull Environ Contam Toxicol 2018;101:692–7.

[58] Goddeti SMR, Bhaumik M, Maity A, Ray SS. Removal of Congo red from aqueous solution by adsorption using gum ghatti and acrylamide graft copolymer coated with zero valent iron. Int J Biol Macromol 2020;149:21–30.

[59] Li B, Yin H. Superior Adsorption property of a novel green biosorbent Yttrium/Alginate gel beads for dyes from aqueous solution. J Polym Environ 2020;28:2137–48.